

***Final Draft***  
**of the original manuscript:**

Kashaev, N.; Venzke, V.; Stepanov, N.; Shaysultanov, D.; Sanin, V.;  
Zherebtsov, S.:

**Laser beam welding of a CoCrFeNiMn-type high entropy alloy  
produced by self-propagating high-temperature synthesis**

In: Intermetallics 96 (2018) 63 - 71

First published online by Elsevier: March 20, 2018

DOI: 10.1016/j.intermet.2018.02.014

<https://dx.doi.org/10.1016/j.intermet.2018.02.014>

# Laser beam welding of a CoCrFeNiMn-type high entropy alloy produced by self-propagating high-temperature synthesis

Nikolai Kashaev<sup>1</sup>, Volker Venzke<sup>1</sup>, Sergey Zherebtsov<sup>2</sup>, Nikita Stepanov<sup>2\*</sup>, Dmitry Shaysultanov<sup>2</sup>, Vladimir Sanin<sup>3</sup>.

<sup>1)</sup>Institute of Materials Research, Materials Mechanics, Department of Joining and Assessment, Helmholtz-Zentrum Geesthacht, Max-Planck-Str.1, 21502 Geesthacht, Germany

<sup>2)</sup>Belgorod State University, Pobeda 85, Belgorod, 308015, Russia

<sup>3)</sup>Institute of Structural Macrokinetics and Materials Science of Russian Academy of Sciences, Academician Osipyan Str., 8, Chernogolovka, Moscow Region, 142432, Russia.

## Highlights:

- CoCrFeNiMn-type high entropy alloy was produced by self-propagating high-temperature sintering
- Laser beam welding of CoCrFeNiMn-type high entropy alloy was successfully achieved
- Microhardness of the weld was considerably higher than that of the base material
- Increase of the microhardness was associated with the precipitation of nanoscale B2 particles

## Abstract:

Autogenous laser beam welding of a CoCrFeNiMn-type high entropy alloy (HEA) produced by self-propagating high-temperature synthesis (SHS) was reported in this work. The SHS-fabricated alloy was characterized by ~2 times reduced Mn content in comparison with the content of the other principal components and the presence of impurities including Al, C, S, and Si. The as-fabricated alloy was composed of columnar fcc grains with coarse precipitates of MnS and fine precipitates of Cr-rich M<sub>23</sub>C<sub>6</sub> carbides. Successful defect-free butt joint of the alloy was obtained using the laser power of 2 kW and the welding speed of 5 m/min. Welding

---

\* Corresponding author: Nikita Stepanov, [stepanov@bsu.edu.ru](mailto:stepanov@bsu.edu.ru); [stepanov.nikita@icloud.com](mailto:stepanov.nikita@icloud.com)

resulted in changes in texture and structure of the fcc matrix. Based on the EBSD analysis the differences were obtained in the image quality values. The lower image quality values for the heat affected zone ( $4105 \pm 1074$ ) and the fusion zone ( $3905 \pm 1139$ ) in comparison to the base material ( $6599 \pm 1167$ ) indicated on the density of defects in fcc matrix increased through the laser beam welding. In addition, precipitation of nanoscale B2 phase particles in the weld zone was observed. A pronounced increase in microhardness from  $153 \pm 3$  HV 0.5 (base material) to  $208 \pm 6$  HV 0.5 (fusion zone) was observed. The B2 phase precipitation after welding was found to be in a reasonable agreement with the ThermoCalc predictions. Quantitative analysis demonstrated that the increase in hardness can be associated with the B2 phase precipitation. Possibilities of the development of HEAs with intrinsic hardening ability after laser processing are discussed.

**Keywords:** Laser beam welding; High entropy alloy, Microstructure, Phase transformation, Microhardness

## 1. Introduction

High entropy alloys (HEAs) have recently emerged as a new class of advanced metallic materials promising for various applications [1–4]. Their main feature is high complexity of chemical composition; according to original definition, HEAs should be composed of at least 5 principal elements in close to equiatomic concentrations (5-35 at.%) [5]. It was proposed that due to such complex composition HEAs can possess structures and properties which cannot be attained in conventional, single element based alloys [1,2,6]. However, vast opportunities for novel alloys development provided by HEAs concept also present a major challenge: a special methodology is required to select promising alloys for specific application out of numerous candidates in a time- and cost-effective way [1,7–9].

One of the promising classes of the HEAs which attained particular attention is fcc-structured Co-Cr-Fe-Ni-Mn system alloys. The equiatomic CoCrFeNiMn alloy was introduced by Cantor et al. in 2004 [10], almost simultaneously and independently from the first paper on HEAs [5]. The alloy was found to have a single fcc phase structure [10–13]. Latter it was revealed that the alloy has unique mechanical properties: very high ductility at room temperature becomes even higher when the temperature decreases into the cryogenic interval. The alloy also has record-

breaking fracture toughness at cryogenic temperature [14–16]. High ductility and toughness were attributed to active nano-twinning under cryogenic conditions [14,15,17,18]. However the alloy has relatively low yield strength [14,16], which limits possible practical applications. Many efforts have been devoted to increase the strength of the CoCrFeNiMn or similar alloys by alloying and/or thermomechanical treatment [14,19–37]. It was found that among the possible strengthening mechanisms (including grain boundary and solid solution strengthening) the most potent one is precipitation hardening. For instance, the yield strength of a  $(\text{CoCrFeNi})_{94}\text{Al}_4\text{Ti}_2$  alloy after proper heat treatment (aging) increases from 503 to 1005 MPa while maintaining sufficient ductility [36].

Although composition-structure-properties relations of the Co-Cr-Fe-Ni-Mn system alloys are under extensive investigation at the moment, many aspects of behaviour of these alloys have not received significant attention yet. For instance development of effective joining technologies is important for potential application of any structural material. But not many information on welding of HEAs is available. Successful electron beam welding of the CoCrFeNiMn alloy without formation of solidification cracking was reported in [38]. After welding, the alloy demonstrated mechanical properties very similar to those of the base material. Application of friction stir welding to  $\text{CoCrFeNiAl}_{0.3}$  was described in [39]. Significant grain refinement and high hardness in the stir zone were observed.

In contrast to the electron beam welding, laser beam welding can be conducted without vacuum by using inert gas shielding, and it has a much higher flexibility in comparison to electron beam welding. However, it is not clear, whether HEAs can be successfully laser beam welded. Recently, laser based processes were only investigated for cladding of HEAs, where the main emphasis was given to produce coatings with advanced properties [40-43]. Therefore the effect of fiber laser beam welding on structure and hardness of the CoCrFeNiMn-type HEA was reported in present study. The initial material was produced by self-propagating high-temperature synthesis (SHS) which recently was found to be capable method for HEAs production [40].

- [40] Y. Cai, Y. Chen, Z. Luo, F. Gao, L. Li, Manufacturing of FeCoCrNiCu<sub>x</sub> medium-entropy alloy coating using laser cladding technology, Mater. Des. 133 (2017) 91-108. doi: 10.1016/j.matdes.2017.07.045.
- [41] F.Y. Shu, L. Wu, H.Y. Zhao, S.H. Sui, L. Zhou, J. Zhang, W.X. He, P. He, B.S. Xu, Microstructure and high-temperature wear mechanism of laser cladded CoCrBFeNiSi high-entropy alloy amorphous coating, Mater. Lett. 211 (2018) 235-238. doi: 10.1016/j.matlet.2017.09.056.
- [42] F.Y. Shu, S. Liu, H.Y. Zhao, W.X. He, S.H. Sui, J. Zhang, P. He, B.S. Xu, J. Alloy. Compd. 731 (2018) 662-666. doi: 10.1016/j.jallcom.2017.08.248.
- [43] Q. Chao, T. Guo, T. Jarvis, X. Wu, P. Hodgson, D. Fabijanic, Direct laser deposition cladding of Al<sub>x</sub>CoCrFeNi high entropy alloys on a high-temperature stainless steel, Surf. Coat. Tech., Article in Press. doi: 10.1016/j.surfcoat.2017.09.072.

## 2. Experimental methods

### 2.1. Material and laser beam welding

The synthesis of initial CoCrFeNiMn-type alloy was carried out with the use of thermite-type SHS powders containing oxides of the target elements (NiO, Cr<sub>2</sub>O<sub>3</sub>, Co<sub>3</sub>O<sub>4</sub>, Fe<sub>2</sub>O<sub>3</sub>, MnO<sub>2</sub>) and Al as the metal reducer. The average particle size was 50–100 µm for the oxides and less than 140 µm for aluminum (brand PA-4). The weight of the initial mixture for combustion was constant in all experiments (1200 g). Combustion was carried out in graphite molds of 80 mm in diameter. The inner surface of the graphite molds was laminated with Al oxide (Al<sub>2</sub>O<sub>3</sub>) to ensure minimal reactive interaction between the form material and metal melt. The synthesis of the program alloy was carried out in a centrifugal SHS setup. The obtained ingot after the synthesis was  $600 \pm 10$  g in weight and had a diameter of 80 mm and height of  $\approx 15$  mm. The fabricated ingot had a weight close to the calculated value (about 98. wt %), and the weight loss (sputtering) of the composition during combustion was no higher than 1.5 wt %. The metallic (target) and oxide (slag) layers after the synthesis were easily mechanically separated into two parts: the target alloy and the oxide layer (Al<sub>2</sub>O<sub>3</sub>).

The coupons for the welding (measured 15 mm × 15 mm × 2 mm) were cut from the ingot produced by SHS by electric discharge machining and subsequently cleaned and ground. The

chemical composition of the raw material (

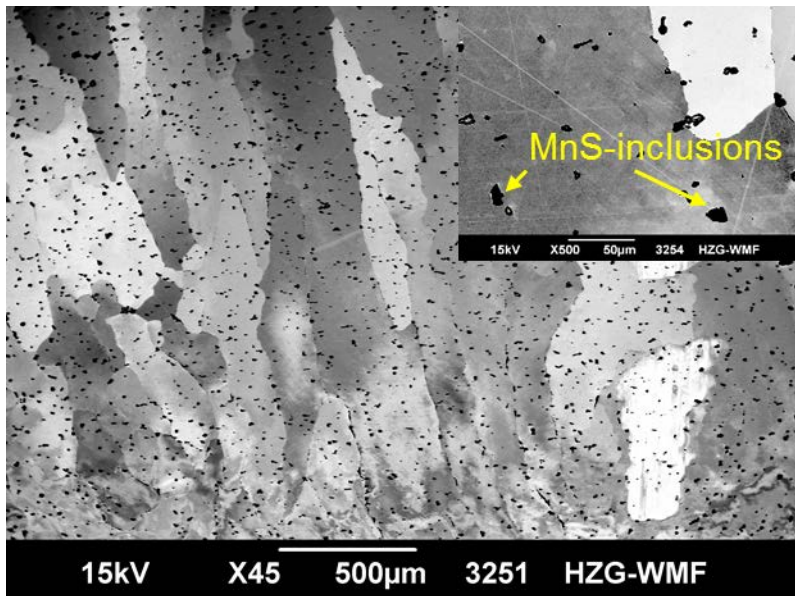


Fig. 1. BSE contrast of BM microstructure.

Table 1) was determined by the energy dispersive X-ray analysis (EDX). Laser beam welding (LBW) of the butt joints was performed using an 8.0 kW fibre laser with a fibre optic (300 μm core diameter) and a 300 mm focal length. Butt joints were welded autogenously in a 3-axis Ixion CNC machine in argon atmosphere. The LBW process was performed using the following process parameters:

- The laser power of 2.0 kW;
- The focus position of 0.0 mm above the specimen surface;
- The welding speed in the range between 3.0 m/min and 6 m/min.

## 2.2. Microstructural characterization and mechanical tests

The specimens for metallographic analysis were prepared by conventional procedures followed by a final polishing with an oxide polish suspension compound (OPS). The specimens were etched prior to optical microscopy investigations to determine the geometrical features of the welds. Visual inspections were also used to analyse the outer appearance of the weld seams to examine for weld imperfections, e.g., underfill, undercut, spatter and excess of penetration.

The microstructures of the laser beam welded butt joints were also investigated using scanning electron microscopy (SEM) (Jeol JSM-6490LV) with electron back-scatter diffraction (EBSD)

(EDAX TSL OIM) to determine the local micro-texture, phase contents and grain sizes. The EBSD measurements were performed at 30 kV, an emission current of 75  $\mu$ A, a sample tilt angle of 70 °, a working distance of 14 mm, a magnification of 100 $\times$  and a step size of 2.0  $\mu$ m. The scan field size was 950  $\mu$ m  $\times$  950  $\mu$ m. The orientation calculation was based on the GSHE method, where triclinic sample symmetry could be assumed. The metallographic samples used for EBSD analysis and microhardness testing were prepared by conventional multi-stage grinding and subsequent vibration polishing.

The samples for TEM analysis were prepared by conventional twin-jet electro-polishing of mechanically pre-thinned to 100  $\mu$ m foils, in a mixture of 95% C<sub>2</sub>H<sub>5</sub>OH and 5% HClO<sub>4</sub> at the 27 V potential. TEM investigations were performed using a JEOL JEM-2100 microscope with accelerating voltage of 200 kV equipped with energy-dispersive X-ray spectroscopy (EDS) detector.

Microhardness profiles across the joint were obtained using an automated Vickers hardness testing machine with a 0.5 kg load.

### 3. Results and Discussion

#### 3.1 Structure and composition of the base material

The microstructure of the alloy produced by self-propagating high-temperature synthesis consisted of dendritic grains containing many inclusions (Fig. 1). The EDX analyses conducted for the base material (BM) and the inclusions (Table 1 and Table 2) detected the following elements: Al, Si, S, Cr, Mn, Fe, Co and Ni (Table 1). The alloy contained ~18-24 wt.% of Co, Cr, Fe, and Ni, 11.03% of Mn, 2.64% of Al, and 0.16-0.23% of S and Si. Although carbon is presented in the alloy (see Section 2.1) it was not detected most possibly due to limited resolution of the used SEM-EDS system. The EDX analysis of inclusions (are seen as dark particles in the BSE-contrast images, Fig. 1) showed that there were MnS-particles (Table 2).

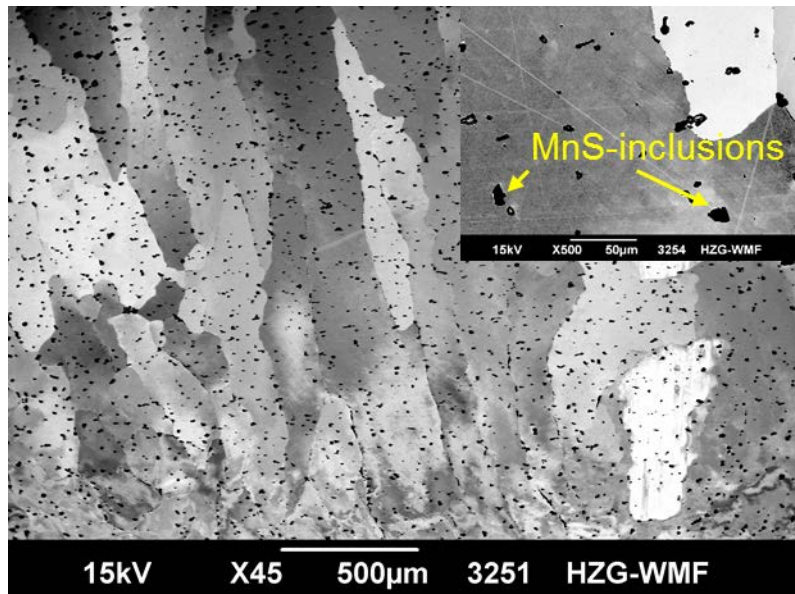


Fig. 1. BSE contrast of BM microstructure.

Table 1. Chemical composition (wt.%) of the investigated high entropy alloy determined by EDX analysis.

Al	Si	S	Cr	Mn	Fe	Co	Ni
2.64	0.16	0.23	18.48	11.03	21.99	21.82	23.65

Table 2. Chemical composition (wt.%) of MnS-inclusions determined by EDX analysis (Indicated with arrows in Fig. 1).

Al	Si	S	Cr	Mn	Fe	Co	Ni
0.15	0.24	18.15	35.46	33.42	6.03	3.67	2.87

As previously mentioned, the BM exhibited a dendritic microstructure with the average major axis length of  $(285.6 \pm 53.2) \mu\text{m}$ , minor axis length of  $(98.4 \pm 17.6) \mu\text{m}$  and the average aspect ratio of  $0.3 \pm 0.1$  (Fig. 2a). An orientation band between  $<103>/\text{ND}$  and  $<229>/\text{ND}$ , as well as  $<111>/\text{ND}$  can be clearly seen (Fig. 2b). The mean misorientation angle was  $35.6^\circ$ . The microstructure also consisted of low-angle grain boundaries.

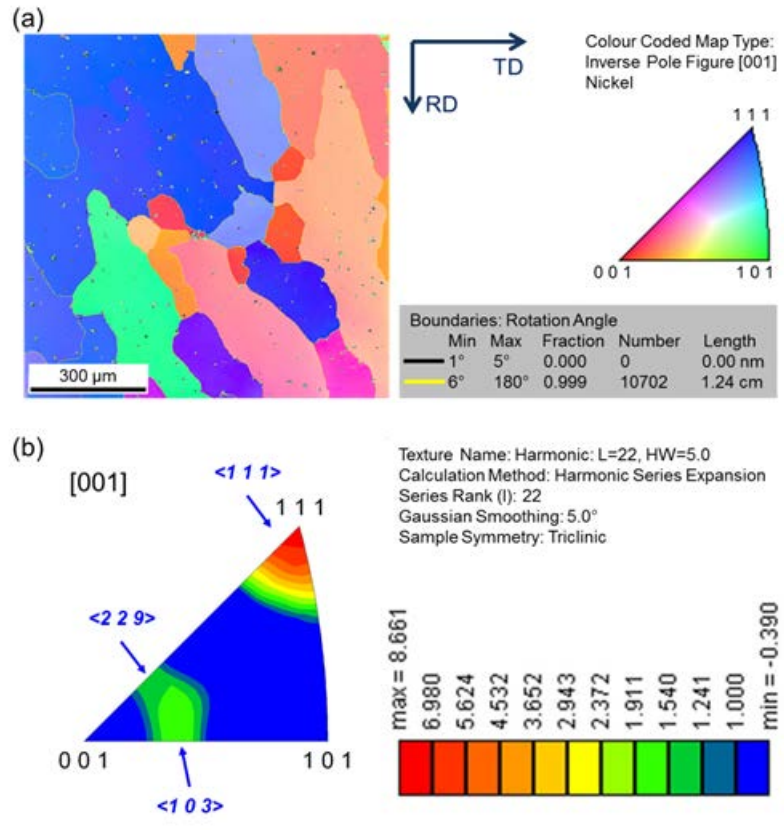


Fig. 2. EBSD analysis of the base material: (a) crystal orientation map and (b) [001] inverse pole figure.

TEM investigations (Fig. 3) demonstrated the presence of rectangular second phase particles with clear interfaces. The average length and width of the particles was  $130 \text{ nm} \pm 60 \text{ nm}$  and  $50 \text{ nm} \pm 20 \text{ nm}$ , respectively. Most of the particles were organized in chains (Fig. 3a). The analysis of the crystal structure of the particles via selected area electron diffraction patterns (SAEDs) has revealed that they were  $\text{M}_{23}\text{C}_6$  type carbides. According to the results of the chemical analysis, the metallic part of the carbides were almost exclusively composed of Cr. Note that the energy resolution of the TEM-EDX system used in current study was insufficient to reliably measure the concentration of carbon due to low atomic weight.

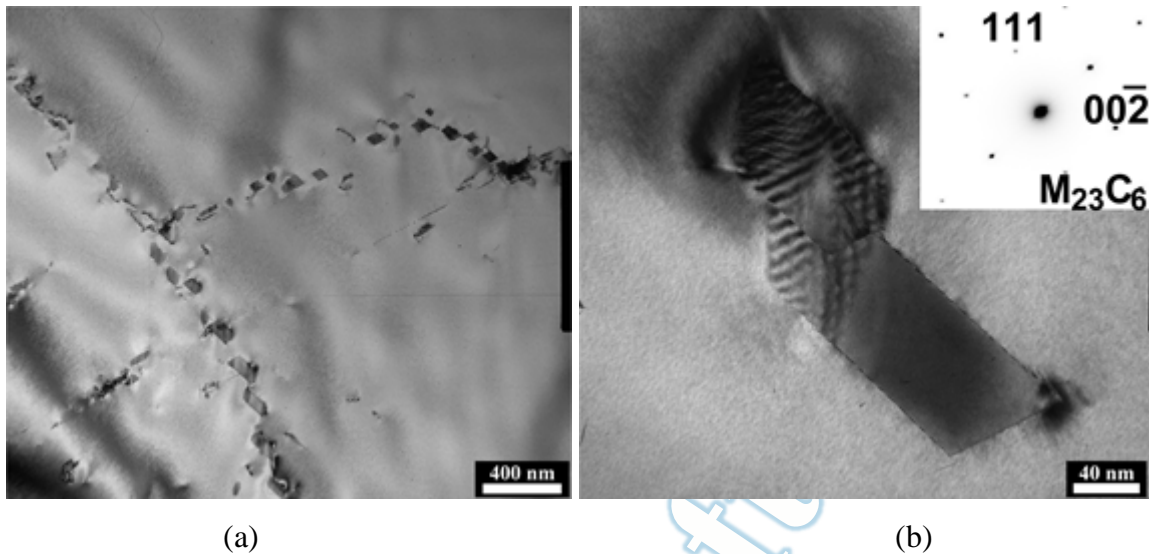


Fig. 3. TEM bright-field images of the base material. Selected area electron diffraction pattern (SAED) of the precipitate is shown in (b).

### 3.2. Structure after the welding

A set of experiments with a laser power level of 2.0 kW and four welding speeds (3.0 m/min, 4.0 m/min, 5.0 m/min and 6.0 m/min) was performed to identify the appropriate welding parameters to produce butt joints with full penetration and regular shapes. During the LBW experiments a formation of welding plume was observed, which indicates the evaporation of the material. This might be the reason for the formation of underfill that is present in the cross-section of the butt joint laser beam welded with a welding speed of 5 m/min (Fig. 4a). The detrimental effect of underfill is that mechanical properties of butt joints can be reduced. The boundary between the joint coupons as well as the boundary of the fusion zone (FZ) are clearly seen in Fig 4a. The weld seam width is  $\sim 570\mu\text{m}$ . Welding defects such as pores or cracks were not identified.

To analyse the influence of the welding speed on the weld shape, the widths of the FZ were measured in the cross-sections of the butt joints at three different positions: radiation exposure side, middle of the weld and weld root side. The results are shown in Fig. 4b. LBW at the welding speed of 3 m/min led to a large FZ width at the radiation exposure side. At the welding speed of 6 m/min the FZ width at the weld root side of  $300\mu\text{m}$  was obtained. An increase of the welding speed above 6 m/min led to a partial penetration, and a decrease of the welding speed below 3 m/min led to a formation of wide weld seam. The results shown in the diagram (Fig 4b)

indicate, that weld with a more “cylindrical” shape (“I”-shape) can be achieved at welding speeds in the range between 4 m/min and 5 m/min. The “cylindrical” shape can be advantageous for tensile properties of the weld.

All butt joints showed non-symmetrical weld shape (Fig. 4a). The reason for the non-symmetrical weld shape might be in coarse columnar grains of the base material. As the butt joint welded at the welding speeds of 5 m/min showed more regular shape this butt joint was used in further microstructural investigations of this study.

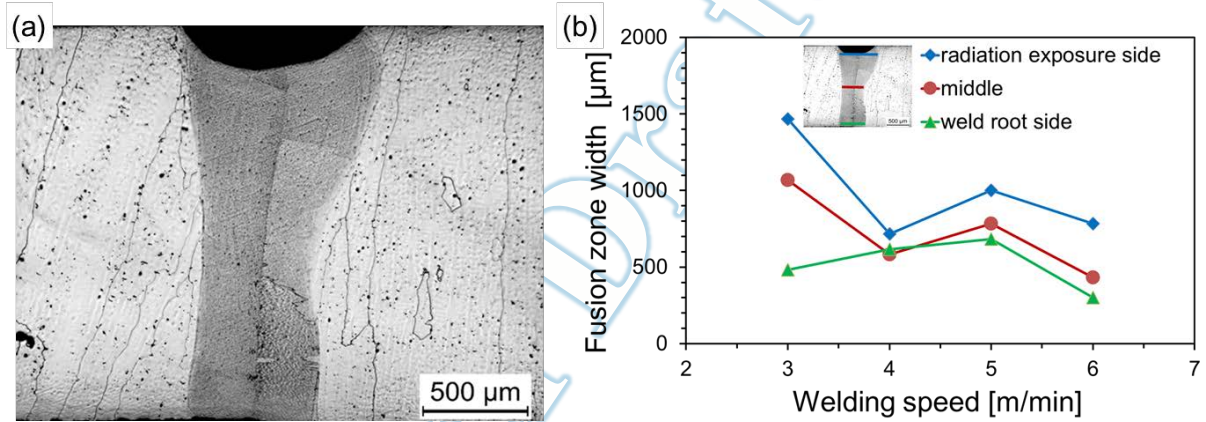


Fig. 4. (a) Macrograph of a butt joint laser beam welded at a laser power level of 2 kW with a welding speed of 5 m/min. (b) FZ width vs. welding speed for butt joints welded at a laser power level of 2 kW.

The difference in microstructure and grain orientation distribution between the BM, heat-affected zone (HAZ) and the fusion zone (FZ) is not significant. Small grains were detected along the solidification front (Fig. 5a). No microstructural transformations were identified. The values of misorientation angles were  $26.7^\circ$  and  $36.9^\circ$  for the HAZ and FZ, respectively. An orientation band  $<103>/\text{ND}$  was observed in the HAZ (Fig. 5b). Changes in the crystal orientation bands were observed in the HAZ/FZ transition area. Also a reduction of axial intensities from 7.2 mrd to 2.8 mrd was presented (Fig. 5c). This is due to the decrease of grain size from the HAZ to the FZ. Figure 5c shows that in FZ grains of smaller size have been generated. The grains show the average major axis length of  $(408.8 \pm 28.0)$  μm and the minor axis length of  $(151.3 \pm 25.6)$  μm with the average aspect ratio of  $0.4 \pm 0.1$  in both cases of HAZ and FZ.

The differences were obtained in the image quality (IQ) values, i.e.,  $\text{IQ} = 6599 \pm 1167$  for the BM,  $\text{IQ} = 4105 \pm 1074$  for the HAZ and  $\text{IQ} = 3905 \pm 1139$  for the FZ (Fig. 6a-c). The IQ value is determined using the contrast and brightness of a Kikuchi diffraction image. The Kikuchi diffraction image is used for the identification of the crystal plane ( $hkl$ ) and determination of the Euler angles ( $\varphi_1, \varphi_2, \varphi_3$ ), which is affected by the density of the defects. The high density of defects reduces the brightness and contrast of the Kikuchi diffraction image and thus the IQ-value. Therefore, the lower IQ-values for the HAZ and the FZ indicate that through the laser beam welding, the density of defects in the fcc matrix increased.

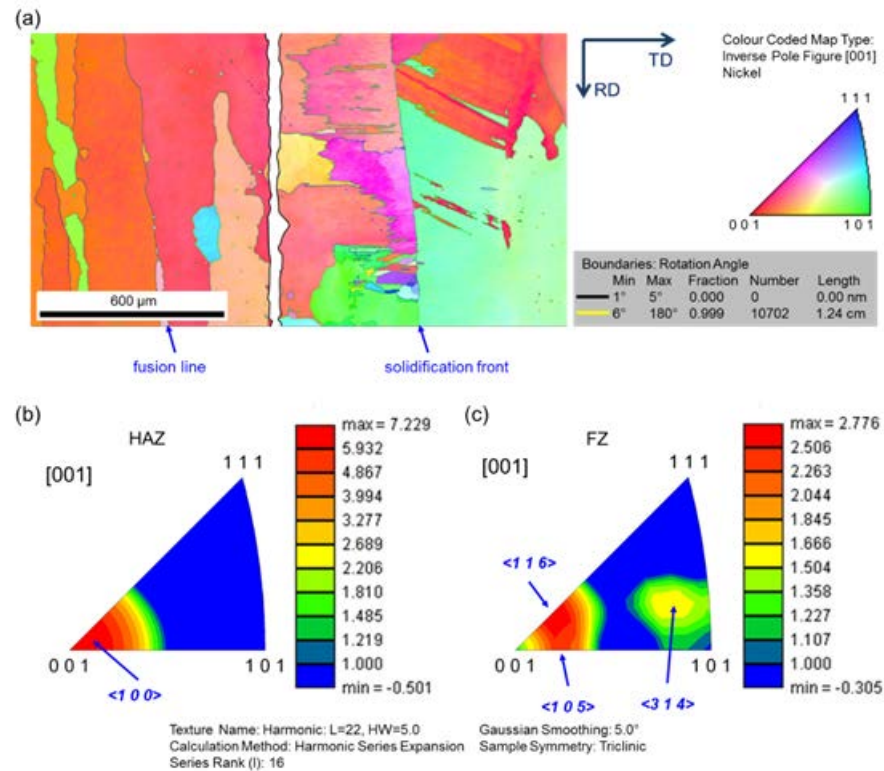


Fig. 5. Butt joint cross section: (a) crystal orientation map and inverse pole figures of (b) HAZ and (c) FZ.

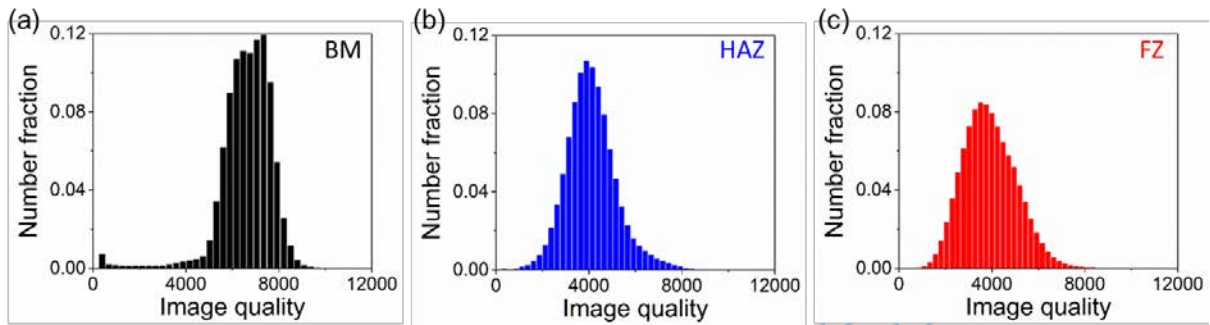
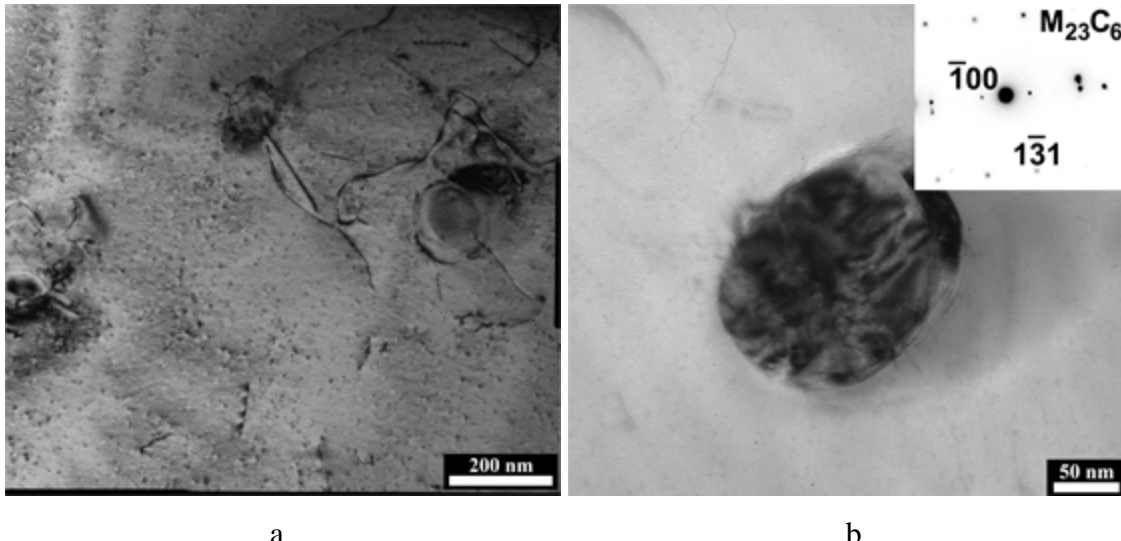


Fig. 6. Number fraction vs. image quality diagrams of (a) BM, (b) HAZ and (c) FZ.

Fig. 6 demonstrates the results of TEM examination of the FZ. Two types of precipitates were found in the fcc matrix (Fig. 6a). The first ones were relatively coarse (average diameter was  $110 \pm 40$  nm)  $M_{23}C_6$  carbides with a nearly spherical shape (Fig. 6b). Their chemical composition did not noticeably differ from the composition of carbides in the base material. The second type of the particles was nano-sized particles with the B2 structure (Fig. 6c,d). Their fraction and the average diameter were ~4% and ~5 nm, respectively. Due to very small size it was impossible to determine reliably the chemical composition of the B2 precipitates by TEM-EDS analysis. However it should be noted, that some B2 precipitate-free areas can be found around carbide particles (Fig. 5b)



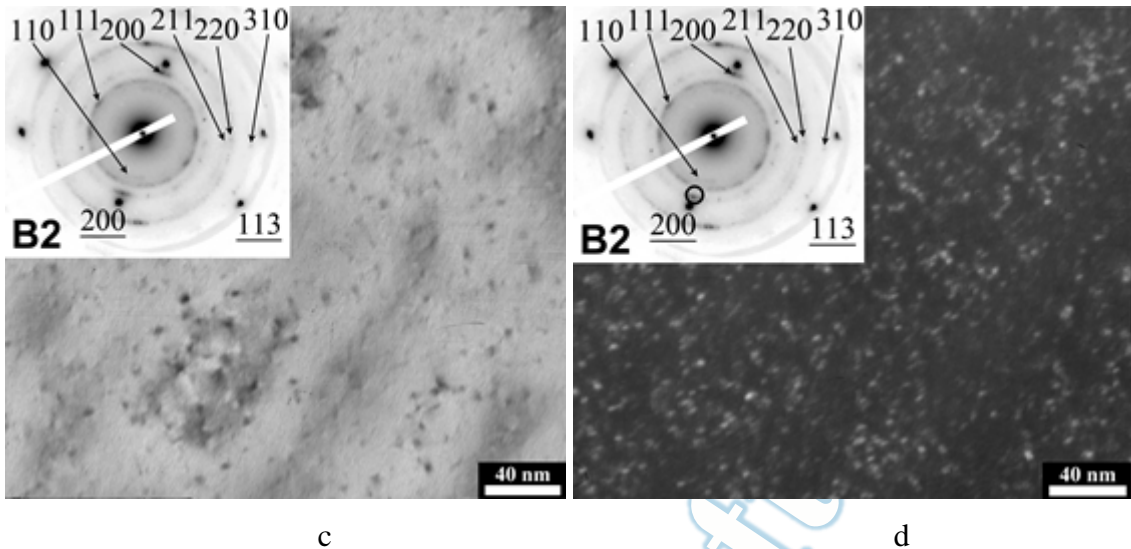


Fig. 6. TEM bright-field (a-c) and dark-field (d) images of the weld joint. Selected area electron diffraction patterns (SAED) of precipitates are shown in (b, c, d).

### 3.3. Microhardness profile

The microhardness profiles were determined across the weld in three regions of the cross-section: the radiation exposure side, middle of the weld and weld root side. An increase in microhardness occurred within the HAZ from the BM to the FZ. The average microhardness values for the BM and FZ are  $153 \pm 3$  HV 0.5 and  $208 \pm 6$  HV 0.5, respectively.

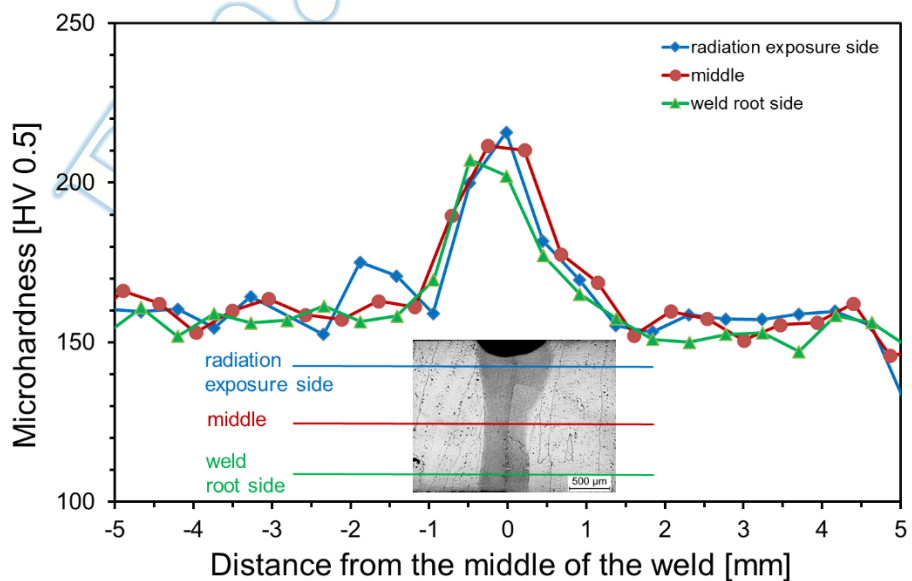


Fig. 6. Microhardness profile of a butt joint laser beam welded at a laser power level of 2 kW with a welding speed of 5 m/min.

#### **4. Discussion**

The presented data shows feasibility of (i) production of the CoCrFeNiMn-type high entropy alloy by self-propagating high-temperature synthesis (SHS) and (ii) successful fiber laser beam welding (LBW) of the produced alloy. The chemical composition of the present alloy differs from that of the well-studied equiatomic CoCrFeNiMn HEA. Also, besides highly anticipated changes in structure and texture of the fcc matrix of the alloy, welding resulted in (i) precipitation of nanoscale B2 phase particles and (ii) significant increase in the microhardness of the FZ. These features will be discussed in details further.

The mentioned difference in chemical composition between the alloy used in current study (Table 1, also contains 0.15 wt.% of C) and the “classical” Cantor’s alloy is most likely associated with the features of SHS. The initial materials for SHS were oxides of the constitutive elements (Co, Cr, Fe, Ni, Mn) and Al<sub>2</sub>O<sub>3</sub> oxide for ignition. The presence of the aluminium oxide in starting powders is most likely the reason of presenting 2.64 wt.% of Al in the alloy (Table 1). Also, Mn is known to be highly volatile element. It can be suggested that approximately a half of Mn was lost during high temperature sintering so that the content of Mn is ~2 times lower than that of other principal metallic elements (Co, Cr, Fe and Ni) (Table 1). In future efforts extra amount of manganese should be used in the initial products to sinter equiatomic alloy via SHS method. The presence of contaminants like C, S, and Si was most likely originated from the impurity of initial oxide powders. Some C can also be introduced from graphite mould although precautions were made not to let it happen.

Formation of the MnS particles can be attributed to highly negative enthalpy of formation of the MnS compound (~ -200 kJ/mol at room temperature [41]). Therefore, it is not surprising that in the alloy with high Mn content ( $\approx$ 11%) in the presence of sulphur (Table 1) MnS inclusions are found. Although the effect of MnS (as well as other inclusions) on mechanical properties of the CoCrFeNiMn-type HEAs has never been studied, MnS are well known as wholesome inclusions in steel products [42,43]. For example Mn is often added to steels to prevent formation of brittle iron sulphides which considerably decrease hot formability [43]. MnS is much softer and therefore does not cause drastic decrease in properties, although crack initiation and propagation is often promoted by these inclusions. The effect of MnS on properties of the CoCrFeNiMn-type alloy will be studied comprehensively in prospective investigations.

A traditional tool for understanding phase formation in metallic alloys is phase diagrams. Unfortunately, experimental phase diagrams for compositionally complex HEAs are mostly unavailable. However equilibrium phase diagrams can be produced using the CALPHAD method. In present work, we have employed ThermoCalc software with recently introduced TCHEA2 database, specifically created for HEAs. However, TCHEA2 database does not include sulphur, and therefore cannot be used for prediction of Mn<sub>2</sub>S particles which were found in the experimental alloy. But Al, C, and Si are included in the database and the presence of second phases caused by these contaminants can be predicted. The constructed phase diagram is shown in Fig. 7.

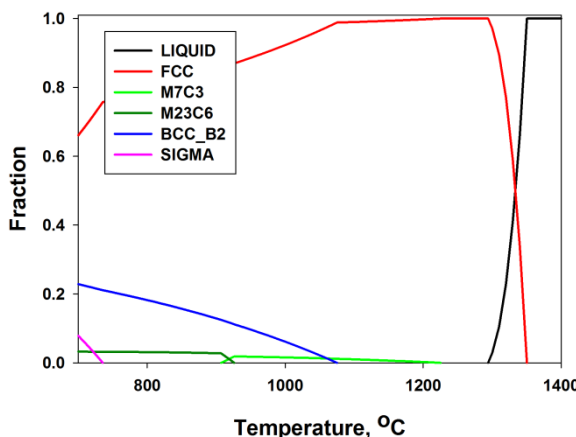


Fig. 7. Calculated equilibrium phase diagram of the program alloy (the composition used for the calculation was (in wt.%) Ni-23.73; Fe-21.99; Co-21.82; Cr-18.48; Mn-11.03; Al-2.64; Si-0.16; C-0.15).

The calculated phase diagram suggests that the alloy solidified through a single fcc phase. The liquidus and solidus temperatures of the alloy were  $\approx 1350^{\circ}\text{C}$  and  $\approx 1290^{\circ}\text{C}$ , respectively. Shortly after solidification, precipitation of M<sub>7</sub>C<sub>3</sub> carbides (the solvus temperature  $\approx 1225^{\circ}\text{C}$ ) was predicted. These carbides can be roughly described as Cr<sub>7</sub>C<sub>3</sub> carbides, as they contain 56-70 (at. %) Cr and 30 (at. %) C. At temperatures in the range 910-925°C M<sub>7</sub>C<sub>3</sub> carbides transformed to M<sub>23</sub>C<sub>6</sub> carbides. The M<sub>23</sub>C<sub>6</sub> carbides were also composed almost exclusively of Cr and C. Nevertheless, the fraction of carbides in the alloy did not increase pronouncedly with decreasing temperature and did not exceed 0.033. At  $\approx 1075^{\circ}\text{C}$  a B2 phase precipitated from the fcc phase as well. This phase was mostly composed of Ni (26-32 at.%) and Al (16-26 at.%). The fraction of this phase increased rapidly with decreasing temperature reaching 0.23 at 700°C. Finally, at 735°C a sigma phase formed. This phase was mostly composed of Cr and Fe and its fraction reached 0.08 at 700°C. Note that Si remained completely dissolved in the fcc phase even at 700°C.

The calculated phase diagram agreed reasonably with the experimental data. For instance, the base (as-sintered) material was composed of the fcc matrix with the  $M_{23}C_6$  carbides ( $MnS$  inclusions were not taken into consideration) (Fig. 1-3). The alloy was predicted to solidify through the single fcc phase field (Fig. 7), but the cooling rate after the SHS process was relatively low (the temperature of the melt after combustion is expected to be high) and thus phase transformations such as precipitation of carbides (predicted to occur only at  $\approx 65^\circ C$  after solidification finishes) were not restricted. Nevertheless, the observed carbides were of  $M_{23}C_6$  type (Fig. 3), while the equilibrium phase diagram suggested the presence of high-temperature  $M_7C_3$  carbides (Fig. 7). The carbides found in the as-sintered alloy were very stable – the remelting of the material during laser welding resulted in their spheroidization only (compare Fig. 3b and Fig. 5b for example). Note that the high-temperature  $M_7C_3$  carbides in the carbon-doped CoCrFeNiMn alloys were found to be stable during low-temperature annealing [22]. Therefore, it is unlikely that the transformation of  $M_7C_3$  into  $M_{23}C_6$  can occur during cooling of the alloy; hence the observed  $M_{23}C_6$  carbides precipitated directly from the fcc solid solution contrary to the thermodynamic prediction. This discrepancy can be attributed to well-known imperfections of the available thermodynamic databases [1].

As it was mentioned earlier welding had an insignificant effect on  $M_{23}C_6$  carbides; meanwhile a plenty of very fine B2 precipitates appeared in the microstructure of the FZ after LBW (Fig. 5). The observed structure of the welded alloy was consistent with the predicted phase fields in the  $735\text{-}910^\circ C$  temperature interval (i.e. the lower-temperature part of the phase diagram (Fig. 7) in comparison with the fcc+carbides phase fields of the sintered alloy). It might seem surprising, as the cooling rates after laser beam welding are expected to be much higher than that after the SHS process. However, one must keep in mind that the temperature of the melted material is likely to be much higher during the SHS process than that during laser welding. Therefore, most probably, the structure of the weld corresponded to equilibrium at relatively low temperature. Fast cooling rates, in turn, should retard diffusion thereby inducing the formation of a very fine B2 precipitates (Fig. 5c and d).

The microhardness of the base material ( $\approx 150$  HV) (Fig. 6) agreed reasonably well with the reported values of the microhardness of the precipitate-free CoCrFeNiMn alloy (160 HV in the as-cast condition [22]). This finding implies that the  $MnS$  inclusions and the  $M_{23}C_6$  carbides found in the as-cast condition of the studied alloy did not cause noticeable strengthening. The latter can be associated with either big size ( $MnS$  inclusions) or low volume fraction and non-random arrangement ( $M_{23}C_6$  carbides) of these phases.

Contrary, the observed phase transformation, i.e. precipitation of the nano-sized B2 particles, can potentially be the reason for the increase of the hardness of the alloy after welding (Fig. 6) to  $\approx 220$  HV. To check this suggestion, the estimation of the strengthening effect of the B2 precipitates was done using the well-known Ashby-Orowan equation [44]:

$$\Delta\sigma = 0.538 G b \left(\frac{\sqrt{f}}{d}\right) \ln \left(\frac{d}{2b}\right) \quad (1)$$

Where  $G$  is the shear modulus,  $b$  is the Burgers vector,  $f$  is the volume fraction of particles, and  $d$  is their diameter. The fraction and diameter of the particles were 0.04 nm and 5 nm respectively. The values of  $G=81$  GPa and  $b=0.254$  nm as reported in [45] for the CoCrFeNiMn equiatomic alloy. After converting the calculated strengthening  $\Delta\sigma$  to HV, we have obtained  $\Delta HV \approx 100$  HV. This value is reasonably close to the experimental increase of microhardness ( $\Delta HV \approx 70$  HV). Possibly, somewhat lower experimental increase of microhardness can be caused by the absence of B2 particles in some areas (Fig. 5b). As a summary, the calculations demonstrate that the increased hardness after laser beam welding can be associated with the precipitation of the nano-sized B2 phase particles.

The obtained results have demonstrated not only feasibility of the SHS process for the fabrication of the CoCrFeNiMn-type HEA and fiber LBW for the effective joining of the alloy, but also pronounced hardness increase in the fusion zone due to the precipitation of the B2 particles. Weld joints are often considered as “weak” areas of fabricated structures, so the higher hardness (strength) in the fusion zone of the laser beam welded CoCrFeNiMn-type alloy can potentially be an advantage for practical application. The important fact is that the hardened joint was produced directly after welding, i.e. no specific post-welding processing was required. It means that the alloy hardens due to the “natural” heat treatment during welding, i.e. melting and rapid cooling. Other laser processing technologies, including additive manufacturing technologies, can benefit from such “intrinsic” hardening [46]. This finding can open the way for designing of HEAs with “intrinsic” hardening capability during laser processing, including, but not limited to, laser beam welding and laser additive manufacturing.

## 5. Conclusion

- 1) CoCrFeNiMn-type high entropy alloy was successfully fabricated using self-propagating high-temperature sintering (SHS) process. The alloy had reduced Mn content and contains impurities including Al, C, S, and Si. Structural investigations had revealed that the alloy was primary composed of coarse columnar grains with fcc structure. Coarse MnS inclusions and fine M<sub>23</sub>C<sub>6</sub> carbides were also found.
- 2) Successful fiber laser beam welding of the CoCrFeNiMn-type high entropy alloy using the laser power of 2 kW was demonstrated. Sound welds without visible defects such as porosity or cracks were produced. The difference in microstructure and grain orientation distribution between the base material, heat-affected zone and the fusion zone was not significant. The EBSD analysis indicated on an increased density of defects in the fcc matrix in the heat affected

zone as well as in the fusion zone in comparison to the base material. In addition, precipitation of the nano-scale (average diameter of 5 nm) B2 phase particles was observed. Formation of B2 precipitates after welding was found to be in reasonable agreement with the equilibrium phase diagram of the alloy produced using ThermoCalc software and TCHEA2 database.

3) Microhardness measurements have revealed significant increase of the microhardness from  $153 \pm 3$  HV 0.5 in the base material to  $208 \pm 6$  HV 0.5 in the fusion zone. The Increase of the microhardness was attributed to the precipitation of the nanoscale B2 particles.

## Acknowledgements

The authors would like to thank Mr. R. Dinse, Mr. P. Haack and Mr. F. Dorn from Helmholtz-Zentrum Geesthacht for their valuable technical support. One of the authors (NDS) would like to acknowledge support from Russian Foundation for Basic Research (grant №16-38-60061).

## References

**Im aktuellen Dokument sind keine Quellen vorhanden.**

- [1] D.B.B. Miracle, O.N.N. Senkov, A critical review of high entropy alloys and related concepts, *Acta Mater.* 122 (2017) 448–511. doi:10.1016/j.actamat.2016.08.081.
- [2] Y. Zhang, T.T. Zuo, Z. Tang, M.C. Gao, K.A. Dahmen, P.K. Liaw, Z.P. Lu, Microstructures and properties of high-entropy alloys, *Prog. Mater. Sci.* 61 (2014). doi:10.1016/j.pmatsci.2013.10.001.
- [3] E.J. Pickering, N.G. Jones, High-entropy alloys: a critical assessment of their founding principles and future prospects, *Int. Mater. Rev.* (2016) 183–202. doi:10.1080/09506608.2016.1180020.
- [4] M.-H. Tsai, J.-W. Yeh, High-Entropy Alloys: A Critical Review, *Mater. Res. Lett.* 2 (2014) 107–123. doi:10.1080/21663831.2014.912690.
- [5] J.-W. Yeh, S.-K. Chen, S.-J. Lin, J.-Y. Gan, T.-S. Chin, T.-T. Shun, C.-H. Tsau, S.-Y. Chang, Nanostructured High-Entropy Alloys with Multiple Principal Elements: Novel

- Alloy Design Concepts and Outcomes, *Adv. Eng. Mater.* 6 (2004) 299–303. doi:10.1002/adem.200300567.
- [6] S. Gorsse, D.B. Miracle, O.N. Senkov, Mapping the world of complex concentrated alloys, *Acta Mater.* 135 (2017) 177–187. doi:10.1016/j.actamat.2017.06.027.
  - [7] D. Miracle, J. Miller, O. Senkov, C. Woodward, M. Uchic, J. Tiley, Exploration and Development of High Entropy Alloys for Structural Applications, *Entropy*. 16 (2014) 494–525. doi:10.3390/e16010494.
  - [8] O.N. Senkov, J.D. Miller, D.B. Miracle, C. Woodward, Accelerated exploration of multi-principal element alloys with solid solution phases, *Nat. Commun.* 6 (2015) 6529. doi:10.1038/ncomms7529.
  - [9] D. Miracle, B. Majumdar, K. Wertz, S. Gorsse, New strategies and tests to accelerate discovery and development of multi-principal element structural alloys, *Scr. Mater.* 127 (2017) 195–200. doi:10.1016/j.scriptamat.2016.08.001.
  - [10] B. Cantor, I.T.H. Chang, P. Knight, A.J.B. Vincent, Microstructural development in equiatomic multicomponent alloys, *Mater. Sci. Eng. A.* 375 (2004) 213–218. doi:10.1016/j.msea.2003.10.257.
  - [11] M. Laurent-Brocq, A. Akhatova, L. Perrière, S. Chebini, X. Sauvage, E. Leroy, Y. Champion, Insights into the phase diagram of the CrMnFeCoNi high entropy alloy, *Acta Mater.* 88 (2015). doi:10.1016/j.actamat.2015.01.068.
  - [12] F. Otto, Y. Yang, H. Bei, E.P.P. George, Relative effects of enthalpy and entropy on the phase stability of equiatomic high-entropy alloys, *Acta Mater.* 61 (2013) 2628–2638. doi:10.1016/j.actamat.2013.01.042.
  - [13] G.A. Salishchev, M.A. Tikhonovsky, D.G. Shaysultanov, N.D. Stepanov, A.V. Kuznetsov, I.V. Kolodiy, A.S. Tortika, O.N. Senkov, Effect of Mn and V on structure

- and mechanical properties of high-entropy alloys based on CoCrFeNi system, *J. Alloys Compd.* 591 (2014) 11–21. doi:10.1016/j.jallcom.2013.12.210.
- [14] F. Otto, A. Dlouhý, C. Somsen, H. Bei, G. Eggeler, E.P. George, The influences of temperature and microstructure on the tensile properties of a CoCrFeMnNi high-entropy alloy, *Acta Mater.* 61 (2013). doi:10.1016/j.actamat.2013.06.018.
  - [15] B. Gludovatz, A. Hohenwarter, D. Catoor, E.H. Chang, E.P. George, R.O. Ritchie, A fracture-resistant high-entropy alloy for cryogenic applications, *Science* (80-. ). 345 (2014). doi:10.1126/science.1254581.
  - [16] A. Gali, E.P. George, Tensile properties of high- and medium-entropy alloys, *Intermetallics*. 39 (2013) 74–78. doi:10.1016/j.intermet.2013.03.018.
  - [17] Z. Zhang, M.M. Mao, J. Wang, B. Gludovatz, Z. Zhang, S.X. Mao, E.P. George, Q. Yu, R.O. Ritchie, Nanoscale origins of the damage tolerance of the high-entropy alloy CrMnFeCoNi, *Nat. Commun.* 6 (2015) 10143. doi:10.1038/ncomms10143.
  - [18] G. Laplanche, A. Kostka, O.M.M. Horst, G. Eggeler, E.P.P. George, Microstructure evolution and critical stress for twinning in the CrMnFeCoNi high-entropy alloy, *Acta Mater.* 118 (2016) 152–163. doi:10.1016/j.actamat.2016.07.038.
  - [19] B. Gludovatz, A. Hohenwarter, K.V.S. Thurston, H. Bei, Z. Wu, E.P. George, R.O. Ritchie, Exceptional damage-tolerance of a medium-entropy alloy CrCoNi at cryogenic temperatures., *Nat. Commun.* (2016). doi:10.1038/ncomms10602.
  - [20] G. Laplanche, A. Kostka, C. Reinhart, J. Hunfeld, G. Eggeler, E.P. George, Reasons for the superior mechanical properties of medium-entropy CrCoNi compared to high-entropy CrMnFeCoNi, *Acta Mater.* (2017). doi:10.1016/j.actamat.2017.02.036.
  - [21] N.D. Stepanov, D.G. Shaysultanov, R.S. Chernichenko, N.Y. Yurchenko, S. V Zherebtsov, M.A. Tikhonovsky, G.A. Salishchev, Effect of thermomechanical

- processing on microstructure and mechanical properties of the carbon-containing CoCrFeNiMn high entropy alloy, *J. Alloys Compd.* (2017). doi:10.1016/j.jallcom.2016.09.208.
- [22] N.D. Stepanov, N.Y. Yurchenko, M.A. Tikhonovsky, G.A. Salishchev, Effect of carbon content and annealing on structure and hardness of the CoCrFeNiMn-based high entropy alloys, *J. Alloys Compd.* (2016). doi:10.1016/j.jallcom.2016.06.103.
- [23] N. Stepanov, M. Tikhonovsky, N. Yurchenko, D. Zyabkin, M. Klimova, S. Zhrebtssov, A. Efimov, G. Salishchev, Effect of cryo-deformation on structure and properties of CoCrFeNiMn high-entropy alloy, *Intermetallics.* 59 (2015) 8–17. doi:10.1016/j.intermet.2014.12.004.
- [24] Z. Wu, C.M. Parish, H. Bei, Nano-twin mediated plasticity in carbon-containing FeNiCoCrMn high entropy alloys, *J. Alloys Compd.* 647 (2015) 815–822. doi:10.1016/j.jallcom.2015.05.224.
- [25] Z. Wu, Y. Gao, H. Bei, Thermal activation mechanisms and Labusch-type strengthening analysis for a family of high-entropy and equiatomic solid-solution alloys, *Acta Mater.* 120 (2016) 108–119. doi:10.1016/j.actamat.2016.08.047.
- [26] Z. Li, C.C. Tasan, H. Springer, B. Gault, D. Raabe, Interstitial atoms enable joint twinning and transformation induced plasticity in strong and ductile high-entropy alloys, *Sci. Rep.* 7 (2017) 40704. doi:10.1038/srep40704.
- [27] Z. Li, K.G. Pradeep, Y. Deng, D. Raabe, C.C. Tasan, Metastable high-entropy dual-phase alloys overcome the strength–ductility trade-off, *Nature.* 534 (2016). doi:10.1038/nature17981.
- [28] N.D. Stepanov, D.G. Shaysultanov, M.A. Tikhonovsky, G.A. Salishchev, Tensile properties of the Cr-Fe-Ni-Mn non-equiatomic multicomponent alloys with different Cr

contents, Mater. Des. 87 (2015) 60–65. doi:10.1016/j.matdes.2015.08.007.

- [29] Z. Wang, I. Baker, Z. Cai, S. Chen, J.D. Poplawsky, W. Guo, The effect of interstitial carbon on the mechanical properties and dislocation substructure evolution in Fe40.4Ni11.3Mn34.8Al7.5Cr6 high entropy alloys, Acta Mater. 120 (2016). doi:10.1016/j.actamat.2016.08.072.
- [30] Z. Wang, I. Baker, W. Guo, J.D. Poplawsky, The effect of carbon on the microstructures, mechanical properties, and deformation mechanisms of thermo-mechanically treated Fe40.4Ni11.3Mn34.8Al7.5Cr6 high entropy alloys, Acta Mater. 126 (2017) 346–360. doi:10.1016/j.actamat.2016.12.074.
- [31] M.J. Yao, K.G. Pradeep, C.C. Tasan, D. Raabe, A novel, single phase, non-equiautomic FeMnNiCoCr high-entropy alloy with exceptional phase stability and tensile ductility, Scr. Mater. 72–73 (2014). doi:10.1016/j.scriptamat.2013.09.030.
- [32] Y. Deng, C.C. Tasan, K.G. Pradeep, H. Springer, A. Kostka, D. Raabe, Design of a twinning-induced plasticity high entropy alloy, Acta Mater. 94 (2015). doi:10.1016/j.actamat.2015.04.014.
- [33] B. Gwalani, V. Soni, M. Lee, S. Mantri, Y. Ren, R. Banerjee, Optimizing the coupled effects of Hall-Petch and precipitation strengthening in a Al0.3CoCrFeNi high entropy alloy, Mater. Des. 121 (2017) 254–260. doi:10.1016/j.matdes.2017.02.072.
- [34] Z. Fu, W. Chen, H. Wen, D. Zhang, Z. Chen, B. Zheng, Y. Zhou, E.J. Lavernia, Microstructure and strengthening mechanisms in an FCC structured single-phase nanocrystalline Co25Ni25Fe25Al7.5Cu17.5 high-entropy alloy, Acta Mater. 107 (2016) 59–71. doi:10.1016/j.actamat.2016.01.050.
- [35] S.J. Sun, Y.Z. Tian, H.R. Lin, X.G. Dong, Y.H. Wang, Z.J. Zhang, Z.F. Zhang, Enhanced strength and ductility of bulk CoCrFeMnNi high entropy alloy having fully recrystallized

- ultrafine-grained structure, Mater. Des. 133 (2017) 122–127.  
doi:10.1016/j.matdes.2017.07.054.
- [36] J.Y.Y. He, H. Wang, H.L.L. Huang, X.D.D. Xu, M.W.W. Chen, Y. Wu, X.J.J. Liu, T.G.G. Nieh, K. An, Z.P.P. Lu, A precipitation-hardened high-entropy alloy with outstanding tensile properties, Acta Mater. 102 (2016) 187–196.  
doi:10.1016/j.actamat.2015.08.076.
- [37] J.Y. He, H. Wang, Y. Wu, X.J. Liu, H.H. Mao, T.G. Nieh, Z.P. Lu, Precipitation behavior and its effects on tensile properties of FeCoNiCr high-entropy alloys, Intermetallics. 79 (2016) 41–52. doi:10.1016/j.intermet.2016.09.005.
- [38] Z. Wu, S.A. David, Z. Feng, H. Bei, Weldability of a high entropy CrMnFeCoNi alloy, Scr. Mater. 124 (2016) 81–85. doi:10.1016/j.scriptamat.2016.06.046.
- [39] Z.G. Zhu, Y.F. Sun, M.H. Goh, F.L. Ng, Q.B. Nguyen, H. Fujii, S.M.L. Nai, J. Wei, C.H. Shek, Friction stir welding of a CoCrFeNiAl 0.3 high entropy alloy, Mater. Lett. 205 (2017) 142–144. doi:10.1016/j.matlet.2017.06.073.
- [40] V.N. Sanin, V.I. Yukhvid, D.M. Ikornikov, D.E. Andreev, N. V. Sachkova, M.I. Alymov, SHS metallurgy of high-entropy transition metal alloys, Dokl. Phys. Chem. 470 (2016) 145–149. doi:10.1134/S001250161610002X.
- [41] J.H.E. Jeffes, F.D. Richardson, J. Pearson, The heats of formation of manganous orthosilicate and manganous sulphide, Trans. Faraday Soc. 50 (1954) 364.  
doi:10.1039/tf9545000364.
- [42] P.A. Thornton, The influence of nonmetallic inclusions on the mechanical properties of steel, J. Mater. Sci. 6 (1971) 347–356. doi:10.1007/BF02403103 T4 - A review M4 - Citavi.
- [43] J. Maciejewski, The Effects of Sulfide Inclusions on Mechanical Properties and Failures

of Steel Components, J. Fail. Anal. Prev. 15 (2015) 169–178. doi:10.1007/s11668-015-9940-9.

- [44] T. Gladman, Precipitation hardening in metals, Mater. Sci. Technol. 15 (1999) 30–36. doi:10.1179/026708399773002782.
- [45] M.J. Jang, D.-H. Ahn, J. Moon, J.W. Bae, D. Yim, J.-W. Yeh, Y. Estrin, H.S. Kim, Constitutive modeling of deformation behavior of high-entropy alloys with face-centered cubic crystal structure, Mater. Res. Lett. 5 (2017) 350–356. doi:10.1080/21663831.2017.1292325.
- [46] P. Kürnsteiner, M.B. Wilms, A. Weisheit, P. Barriobero-Vila, E.A. Jägle, D. Raabe, Massive nanoprecipitation in an Fe-19Ni-xAl maraging steel triggered by the intrinsic heat treatment during laser metal deposition, Acta Mater. 129 (2017) 52–60. doi:10.1016/j.actamat.2017.02.069.